Tellurium-bridged two-leg spin ladder in Ba$_2$CuTeO$_6$

G. Narsinga Rao,[1] R. Sankar,[1,2] Akansha Singh,[3] I. Panneer Muthuselvam,[1] W. T. Chen,[1] Viveka Nand Singh,[4,5]
Guang-Yu Guo,[4,6,*] and F. C. Chou[1,7,8,†]

[1]*Center for Condensed Matter Sciences, National Taiwan University, Taipei 10617, Taiwan*
[2]*Institute of Physics, Academia Sinica, Taipei 10617, Taiwan*
[3]*Harish-Chandra Research Institute, Allahabad 211019, India*
[4]*Department of Physics, National Taiwan University, Taipei 10617, Taiwan*
[5]*Institute of Atomic and Molecular Sciences, Academia Sinica, Taipei 10617, Taiwan*
[6]*Physics Division, National Center for Theoretical Sciences, Hsinchu 30013, Taiwan*
[7]*National Synchrotron Radiation Research Center, Hsinchu 30076, Taiwan*
[8]*Taiwan Consortium of Emergent Crystalline Materials, Ministry of Science and Technology, Taipei 10622, Taiwan*

We present single-crystal growth and magnetic property studies of tellurium-bridged copper spin-$\frac{1}{2}$ system Ba$_2$CuTeO$_6$. The spin-exchange interaction among copper spins via Cu-O-Te-O-Cu super-superexchange route leads to a novel two-leg spin ladder system. Spin susceptibility $\chi(T)$ data indicate that the triclinic Ba$_2$CuTeO$_6$ undergoes a stepwise crossover for exchange couplings revealed by a broad maximum of $\chi(T)$ near $T_{\max}\sim75$ K and an anisotropic cusp in $\frac{d\chi}{dT}(T)$ at $T_N \sim 15$ K to signify a three-dimensional (3D) antiferromagnetic long-range ordering (LRO). The 3D LRO has been suggested from the anisotropic behavior of $\chi(T)$ with strong c-axis spin anisotropy and the signature of spin-flop transition from the isothermal magnetization below T_N. Analysis of magnetic heat capacity (C_m) at $T_N \sim 15$ K indicates that most of the spin entropy ($\sim 92\%$) has already been released above T_N, which supports the picture of consecutive spin entropy reduction upon cooling with Te-bridged two-leg spin ladder system with strong intraladder and interladder couplings. Theoretical DFT+U calculations have been performed to search for the ground-state magnetic configuration and also to evaluate exchange-coupling constants that support the magnetic model deduced from the combined spin susceptibility and crystal structure symmetry analysis.

I. INTRODUCTION

Low-dimensional magnetism of the copper-based quantum spin-$\frac{1}{2}$ system is the foundation to understand high-T_c superconductivity [1]. While most of the high-T_c cuprate superconductors contain electron or hole-doped CuO$_2$ planes of antiferromagnetic (AF) coupling in the normal state, such as the YBa$_2$Cu$_3$O$_7$ of $T_c \sim 93$ K [2], the resonant valence bond (RVB) type bonding mechanism and the Cu-O-Cu spin superexchange (SE) coupling have been examined through many comparative studies of cuprate with various crystal and spin structures [3–5]. The spin structures have been analyzed from one-dimensional (1D) chain to two-dimensional (2D) plane extensively based on the Heisenberg and t-J models [6]. For example, the Sr$_2$CuO$_3$ with Cu-O network of corner-sharing chain [7–9], the CuGeO$_3$ with edge-sharing chain [10], the Sr$_{0.4}$Ca$_{13.6}$Cu$_{24}$O$_{41}$ with two-leg spin ladder [11], the SrCu$_2$O$_3$ and Sr$_2$Cu$_3$O$_5$ with even- and odd-leg spin ladders [12,13], and the multiple number of CuO$_2$ planes per unit cell [14]. Following the development of W- or Te-bridged transition-metal (M) oxides containing spin chain and plane systems, such as Li$_2M$(WO$_4$)$_2$ and A_2MBO$_6$, where $A =$ Sr or Ba, and $B =$ Te or W [15–18], the original SE interaction route of M-O-M has been modified via a Cu-O-(W,Te)-O-Cu of super-superexchange (SSE) interaction route. If two compounds of identical structure but of different

SE and SSE origins, which may not be distinguishable within the theoretical Heisenberg Hamiltonian description, it would be interesting to have a chance to compare the impact of SSE on the spin-coupling forms of spin dimerization, AF ordering, and superconductivity.

Tellurates, oxides containing the Te^{6+} cation, can often be utilized to build three-dimensional crystal structures attributable to their preferred octahedral coordination environment and their ability to bond a large number of metal centers [19–21], as a result, tellurates rarely form low-dimensional crystal structures. In contrast, cuprate compounds have a rich variety of coordination environments, including square planar, square pyramidal, and tetragonally distorted octahedral coordinations. As a result, tellurium-bridged cuprate is a new class of material with a higher degree of freedom on both crystal and magnetic structure variations. Among the few reported examples of tellurium-bridged cuprate compounds, e.g., oxides containing d^9-Cu^{2+} and Te^{6+} cations, such as Sr$_2$CuTeO$_6$ [22], Ba$_2$CuTeO$_6$ [17], Na$_2$Cu$_2$TeO$_6$ [23,24], Tl$_4$CuTeO$_6$, and Tl$_6$CuTe$_2$O$_{10}$ [25], all exhibit three-dimensional crystal structures by using Te as the bridging ion for the spin coupling in SSE form. Interestingly, Na$_2$Cu$_2$TeO$_6$ shows Cu spin dimers that are bridged by the TeO$_6$ octahedra, i.e., the Cu spin dimer has Cu-O-Cu of SE mechanism, but the interdimer coupling is of SSE mechanism. The mixed SE and SSE mechanisms for the tellurium-bridged cuprate compounds open up a new territory in the study of low-dimensional magnetism.

The Ba$_2$CuTeO$_6$ compound exhibits two phases: one is prepared at ambient pressure and the other can only be synthesized under high pressure. A sample prepared at 900 °C
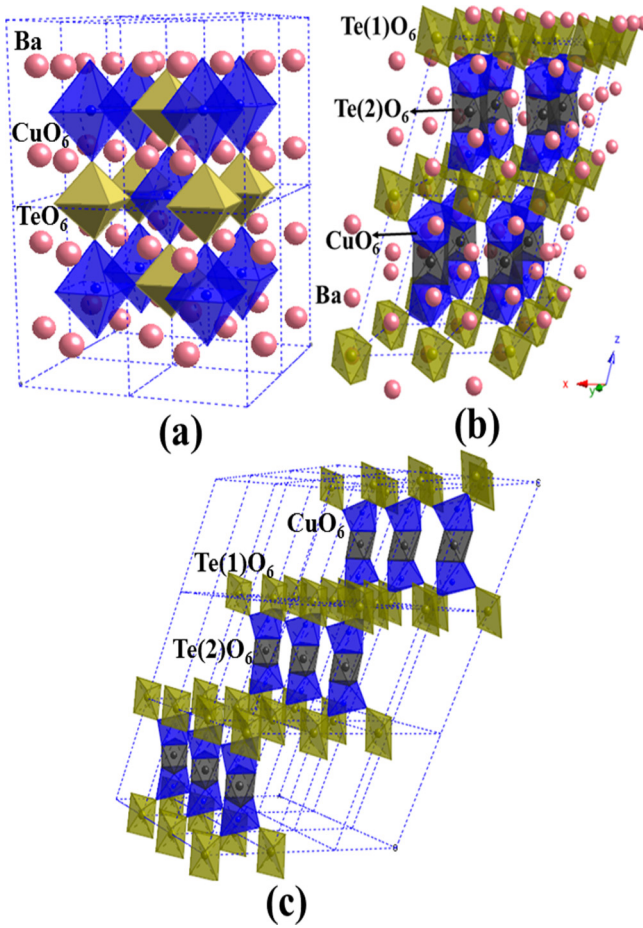
*gyguo@phys.ntu.edu.tw
†fcchou@ntu.edu.tw

FIG. 1. (a) Crystal structure of tetragonal Ba_2CuTeO_6 high-pressure phase. (b) Crystal structure of triclinic Ba_2CuTeO_6 is shown with CuO_6 (blue), $Te(1)O_6$ (yellow), and $Te(2)O_6$ octahedra (black) stacked in layers and the Ba atoms are big sphere (maroon). (c) Single layer of a two-leg spin ladder is illustrated in triclinic Ba_2CuTeO_6, where $Te(2)O_6$ and $Te(1)O_6$ bridge two CuO_6 octahedra via face sharing and corner sharing of oxygen, respectively.

under 5 GPa pressure crystallizes in a perovskite-type structure of tetragonal distortion [Fig. 1(a)] [17], which shows a broad peak of $\chi(T)$ near 175 K to indicate a short-range antiferro-magnet coupling without detectable three-dimensional (3D) long-range magnetic ordering down to ∼2 K. The short-range AF coupling was attributed to the cooperative Jahn-Teller distortion of CuO_6 octahedra. On the other hand, the ambient pressure form crystallizes in a triclinic structure [Fig. 1(b)] [26]. In the triclinic Ba_2CuTeO_6, the distortion of the CuO_6 octahedra is small compared to that of the high-pressure perovskite phase. A detailed study on the triclinic Ba_2CuTeO_6 is desirable to learn more about the dimensionality and the role of bridging Te in the $S = \frac{1}{2}$ quantum spin systems. In addition, physical properties of the triclinic Ba_2CuTeO_6 have not been reported so far, not to mention that using a single-crystal sample.

In this paper, we present the investigation of the thermodynamic and magnetic properties of triclinic Ba_2CuTeO_6 with single-crystal samples. Based on strong SSE coupling of Cu^{2+} spins within the *ab* plane, short-range AF exchange

correlations were found to appear as indicated by the existence of a broad peak of $\chi(T)$ at $T_{max} \sim 75$ K. Moreover, a long-range AF-like anomaly of $T_N = 15$ K has been identified from the cusp in the $d\chi/dT$ plot. These characteristic anomalies were also confirmed in C_P measurements. Based on the unique geometric coordination between CuO_6 and TeO_6 octahedra, we find that these signatures of magnetic coupling shown in the experimental results of $\chi(T)$ and $C_P(T)$ could be attributed to the consecutive short-range AF spin-exchange couplings from the intrachain and interchain interactions of a two-leg spin ladder with nontrivial interladder interactions, which eventually falls to a 3D long-range AF ordering of Cu spins below T_N. These experimental results were found to be consistent with the theoretical calculations within the framework of the density functional theory (DFT).

II. EXPERIMENTAL AND COMPUTATIONAL DETAILS

For the first step of the single-crystal growth, the Ba_2CuTeO_6 polycrystalline sample was prepared by the solid-state reaction method. Stoichiometric proportions of high-purity $BaCO_3$, CuO, and TeO_2 powders were mixed and fired in the air at 1000 °C for 12 h with a heating and cooling rate of 120 °C/h. The preheated powders were well grounded and reheated at 1100 °C for 24 h with several intermediate grindings to reach single phase. The Ba_2CuTeO_6 single crystal was grown with flux method using $BaCl_2$ as the flux. The mixture of the polycrystalline sample of Ba_2CuTeO_6 and the flux of $BaCl_2$ in molar ratio of 1:3 was melted in an alumina crucible at 1150 °C for 24 h. The furnace was slowly cooled to 850 °C at the rate of 3 °C/h and then cooled down to room temperature at the rate of 80 °C/h. Dark green crystals (1–3 mm) were mechanically separated from the crucible and further washed with hot water. The crystal structure and phase purity of the samples were checked by synchrotron x-ray powder diffraction (SXRD) using an incident wavelength of $\lambda = 0.619\,927$ Å (BL01C2, NSRRC, Taiwan). The field-cooled (FC) and zero-field-cooled (ZFC) magnetization curves were measured in a commercial Vibrating Sample Magnetometer (VSM, Quantum Design, USA) from 1.8 to 350 K in the presence of various applied magnetic fields. The isothermal magnetization (*M*) data were also recorded at selected temperatures. The heat-capacity (C_P) measurements were carried out by a relaxation method using the Physical Properties Measurement System (PPMS, Quantum Design, USA).

All theoretical calculations were performed within the framework of the density functional theory (DFT). Interaction between the valence electrons and the ion cores is represented by the projector augmented wave (PAW) potentials [27] as implemented in the Vienna *ab initio* simulation package (VASP) [28,29]. The generalized gradient approximation (GGA) [30] is used for the exchange-correlation functional. The wave functions were expressed in a plane-wave basis set with an energy cutoff of 500 eV and the self-consistent field energies are converged up to 10^{-6} eV. In order to describe the electron-electron correlation associated with the 3*d* states of Cu, the GGA plus onsite repulsion (GGA $+U$) [31] calculations are carried out with an effective $U_{eff} = (U - J) = 3.6$ eV. We note that $LiCu_2O_2$ as a low-dimensional AF oxide with frustrated

exchange couplings, the $U_{\text{eff}} = (U - J) = 3.6$ eV used in the previous GGA $+U$ calculation is in good agreement with that extracted from the x-ray absorption experiment [32]. Therefore, we used the same U_{eff} for Cu atoms in the present GGA$+U$ calculations for Ba_2CuTeO_6.

The crystal structure data for the *ab initio* calculations were taken from the refined experimental lattice parameters. The primitive unit cell of Ba_2CuTeO_6 contains two formula units, i.e., there are two Cu atoms per unit cell. In order to investigate the magnetic ground state of this system, we have considered a $(2 \times 2 \times 2)$ supercell. In the present calculations, we used the tetrahedron method with Blöchl corrections for the Brillouin zone integration with a Γ-centered Monkhorst-Pack k-point mesh of $(6 \times 6 \times 3)$. Further test calculations using denser k-point meshes and larger kinetic energy cutoffs showed that the calculated total energy differences of the magnetic states considered with respect to the ferromagnetic state converged well to within 10^{-4} eV.

To ensure that the structural parameters from the present theoretical calculations are not significantly different from the experimental ones, we have also determined both the lattice constants and atomic positions theoretically. First, we calculated the total energy for several sets of lattice constants and fit them to a volume (V) polynomial of total energy $E = a_0 + a_1 V + a_2 V^2 + a_3 V^3$. The thus-obtained theoretical lattice constants are quite close to the experimental ones (being about 2% larger). Then, we optimized the atomic structure using the theoretical lattice constants. In the structural optimization, atoms are allowed to relax until the forces on the atoms are smaller than 0.01 eV/Å. We found that the calculated bond lengths and bond angles differ from the corresponding experimental values by only a few percent. Therefore, to have better agreement with the experiments, we present only the results of our *ab initio* calculations using the refined experimental structural parameters in this paper.

III. RESULTS AND DISCUSSION

A. Crystal structure

The powder SXRD pattern of the polycrystalline Ba_2CuTeO_6 is shown in Fig. 2(a). The SXRD pattern can be indexed with a space group of $P\bar{1}$ in triclinic symmetry without any observable trace of impurity phases. The structural parameters were refined by the general structure analysis system (GSAS) program [33] following the Rietveld technique of satisfactory quality as indicated by the $R_{wp} = 5.06\%$ and $R_p = 3.79\%$. The fitted lattice parameters are $a = 5.7288(1)$ Å, $b = 5.8677(1)$ Å, and $c = 10.2237(2)$ Å, $\alpha = 107.867(1)°, \beta = 106.208(2)°$, and $\gamma = 60.750(2)°$, which are in good agreement with previously reported values [26]. The single-crystal diffraction pattern shows only $(00l)$ reflections [Fig. 2(b)], indicating the preferred ab-plane orientation of the as-grown crystal. Single crystals were obtained in the form of hexagonal geometric shapes as shown in the inset of Fig. 2(b). The ordered Ba_2CuTeO_6 could be viewed consisting of CuO_6 octahedra which are bridged through TeO_6 octahedra in either face sharing [for Te(2)] or corner sharing [for Te(1)], as shown in Fig. 1(b). Alternatively, Ba_2CuTeO_6 can also be viewed

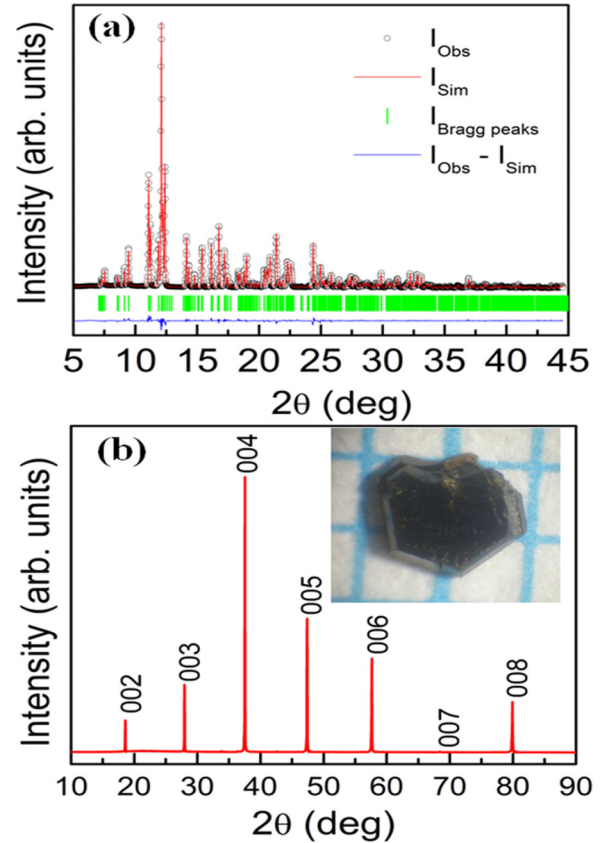FIG. 2. (a) Room-temperature powder SXRD pattern of Ba_2CuTeO_6, where black circles are experimental data, solid curve in red is the best fit from the Rietveld refinement. The vertical bars indicate the position of Bragg peaks of space group $P\bar{1}$ and the bottom curve shows the difference between the observed and calculated intensities. (b) Single-crystal diffraction pattern obtained using an x-ray (Cu-K_α) beam perpendicular to the ab plane. Inset shows a photograph of grown single crystal.

composing of Te(2)-bridged Cu dimers through the SSE route, as illustrated in Fig. 1(c).

B. Magnetic susceptibility

Figure 3(a) shows the homogeneous magnetic susceptibility $(\chi = M/H)$ of single-crystal Ba_2CuTeO_6 as a function of temperature $\chi(T)$ measured in an applied magnetic field of 10 kOe along $(H\|)$ and perpendicular $(H\perp)$ to the ab plane, which shows an approximation to the actual c axis when the actual crystal symmetry is triclinic of pseudohexagonal shape [inset of Fig. 2(b)] with α and β angles are not in right angles but close to $100°$. There was no detectable difference between data taken through the field-cooled (FC) and zero-field-cooled (ZFC) routes. As the temperature was lowered, an isotropic broad maximum of $\chi(T)$ at $T_{\max} \sim 75$ K was observed, presumably due to AF-like short-range exchange correlations. Below about ~ 15 K, $\chi(T)$ measured at 10-kOe data were found anisotropic, which was confirmed with a low field of 100 Oe to indicate the onset of an AF-like long-range ordering (LRO), as shown in the lower inset of Fig. 3(a).
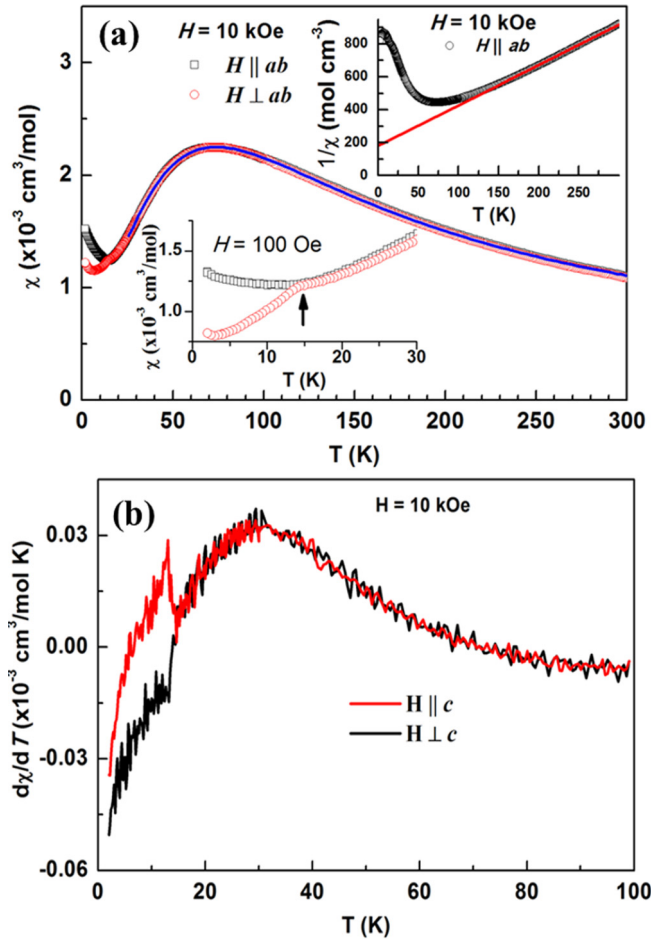
FIG. 3. (a) The temperature dependence of magnetic susceptibility measured in an applied magnetic field of 10 kOe for $H\|ab$ and $H\perp ab$ of Ba_2CuTeO_6 single crystal. The solid curve in blue is the best fit from the modified Bonner-Fisher AFM chain model. Upper inset shows $1/\chi(T)$ fitted to the Curie-Weiss law (solid red line). The low-field $\chi(T)$ curve below 30 K is displayed in the lower inset with a transition temperature near ~ 15 K as indicated by the arrow. (b) The $d\chi/dT$ vs T curves measured with field of 10 kOe reveal an anisotropic cusp of $T_N \sim 15$ K.

By taking the temperature derivative of $\chi(T)$ measured at 10 kOe, as shown in Fig. 3(a), the $\frac{d\chi}{dT}(T)$ curves reveal more distinct anomaly below $T_{max} \sim 75$ K, a cusp of $d\chi/dT$ that suggests a sharp drop of $\chi(T)$ near $T_N \sim 15$ K, as illustrated more clearly in Fig. 3(b). The broad maximum of $\chi(T)$ at $T_{max} \sim 75$ K indicates the existence of a short-range AF exchange correlation, as commonly found in the Cu-O chain or plane systems of superexchange spin coupling [34,35]. While the $d\chi/dT$ cusp corresponds to the anisotropic sharp drop of $\chi(T)$, $T_N \sim 15$ K strongly suggests the onset of a long-range AF-like spin ordering with spins oriented mostly perpendicular to the ab direction, either as an AF or a helical ordering type. A detailed spin structure requires further neutron diffraction study.

The high-temperature part ($T \geqslant 150$ K) of the $\chi(T)$ data shows a paramagnetic behavior and can be fitted with the Curie-Weiss law [$\chi(T) = \chi_0 + \frac{C}{T-\Theta}$] satisfactorily as shown solid red line in the upper inset of Fig. 3(a). The obtained

fitting parameters are $\chi_0 \simeq 1.02 \times 10^{-4}$ cm^3/(mol Cu), $C = N_A g^2 \mu_B^2 S(S+1)/3k_B \simeq 0.368$ cm^3 K (mol Cu)$^{-1}$, and $\Theta \simeq -63$ K, where N_A, g, μ_B, k_B, and Θ represent Avogadro number, Lande-g factor, Bohr magneton, Boltzmann constant, and the Curie-Weiss temperature, respectively. The core diamagnetic susceptibility (χ_{dia}) of Ba_2CuTeO_6 is estimated to be -1.12×10^{-4} cm^3/mol per formula unit from the corresponding ions of Ba^{2+}, Cu^{2+}, Te^{2+}, and O^{2-} [36]. The estimated Van Vleck paramagnetic susceptibility χ_{vv}, i.e., after χ_0 is corrected with the core diamagnetic contribution (χ_{dia}), is found to be $\simeq 2.14 \times 10^{-4}$ cm^3/mol, which is of similar magnitude to other cuprates [37–39]. The estimated effective magnetic moment (μ_{eff}) of Cu^{2+} is $\sim 1.72\,\mu_B$, which is close to the theoretical spin-only value of Cu^{2+} ($S = \frac{1}{2}$) ions ($\mu_{eff} = 1.73\,\mu_B$).

Below 150 K, deviation from the Curie-Weiss law occurs and develops into a broad maximum in $\chi(T)$ near $T_{max} \sim 75$ K, which indicates the existence of a short-range spin-exchange correlation. An attempt has been made to fit the data to the modified Bonner-Fisher AFM chain model that includes a parameter J_{inter} to account for the interchain interactions [40,41], as shown in Eq. (1) and in series expansion form of Eq. (2), which provided a satisfactory fit as shown by the solid blue line in the main panel of Fig. 3(a). The obtained fitting parameters are $g = 2.07$, the intrachain exchange coupling $J = 48.6$ K, and the average interchain exchange coupling $J_{inter} = 22.8$ K between Cu^{2+} spins:

$$\chi_{chain} = \frac{\chi_{BF}}{1 - \frac{2(J_{inter})\,\chi_{BF}}{N_A\,g^2\,\mu_B^2}}, \qquad (1)$$

$$\chi_{BF} = \frac{N_A\,g^2\,\mu_B^2}{k_B\,T}\frac{0.25 + 0.14995\,x + 0.30094\,x^2}{1.0 + 1.9862\,x + 0.68885\,x^2 + 6.0626\,x^3}, \qquad (2)$$

where $x = |J|/k_B T$.

We present our magnetization data as a function of magnetic field H along the two crystal orientations $H \parallel ab$ and $H \perp ab$ plane in Fig. 4(a). Magnetization isotherms at 2 K with magnetic field up to 70 kOe were obtained, where no field or temperature hysteresis is observed. A clear step increase of $M(H, T = 2$ K$)$ is observed in the range near ~ 10–20 kOe for $H \perp ab$ only, as also shown in Fig. 4(b) for its derivative. The significant increase of dM/dH [Fig. 4(b)] above the critical field strongly suggests the occurrence of a spin-flop transition, i.e., the enhanced spin susceptibility at higher field for $H \perp ab$ could be resulted from the magnetic field induced spin-flop transition so that spin direction of the AF ordered spins is flopped from its original $\perp ab$ direction to the $\parallel ab$ direction [42]. Moreover, dM/dH curves [inset of Fig. 4(b)] do not show the spin-flop transition above ~ 15 K. These results are consistent to the proposal that a long-range AF spin ordering has occurred below $T_N \sim 15$ K and the spin anisotropy is near the $\perp ab$ direction, which agrees with the observation that $\chi(T)$ reduction below $T_N \sim 15$ K is observed along the $\perp ab$ direction [see Fig. 3(a)].

C. Heat capacity

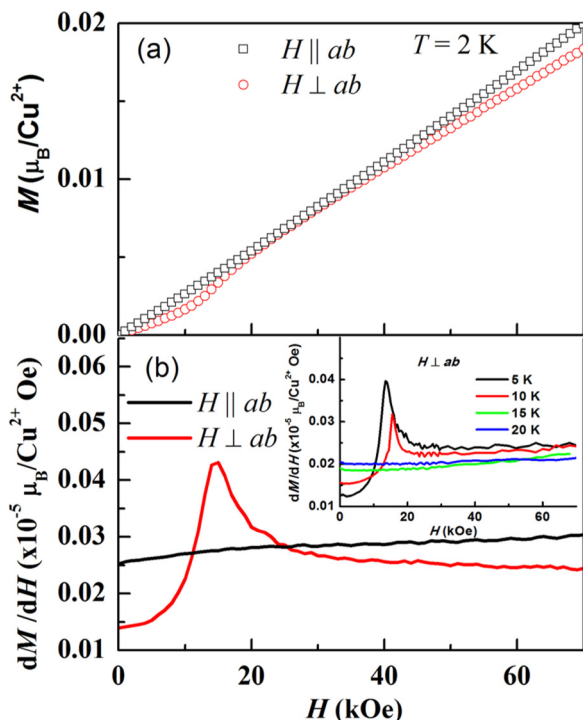The heat-capacity $C_P(T)$ measurement results for Ba_2CuTeO_6 single crystal at zero field are presented in

FIG. 4. (a) The field dependence of magnetization at 2 K for $H \parallel ab$ and $H \perp ab$, the first derivative of $M(H)$ for both directions are shown in (b) with an inset to illustrate the dM/dH across the T_N in $H \perp ab$.

FIG. 5. (a) The temperature dependence of the total heat capacity (C_P/T) for Ba_2CuTeO_6 single crystal. Inset shows the C_P/T^2 vs T curve. The arrows indicating the corresponding characteristic temperatures of T_{max} and T_N. (b) C_m/T vs T and the entropy change ΔS as a function of temperature, where C_m is derived from total C_P with lattice contribution subtracted. The ΔS at T_N corresponds to about 8% of the total Cu spin entropy of $R\ln 2 \sim 5.76 J/(\text{mol K})$ for $S = \frac{1}{2}$. The red solid line shows the heat capacities derived from the spin-wave theory, as described in the text.

Fig. 5(a). It is also found that the $C_P(T)$ data for 30 kOe coincide with the zero-field data (not shown here). As shown in the plot of C_P/T, no significant λ-type peak attributable to a long-range magnetic ordering is found down to 2 K. On the other hand, the C_P/T curve exhibits a broad maximum at ~ 75 K, as shown in Fig. 5(a), which is consistent with the $\chi(T)$ maximum near $T_{max} \sim 75$ K. A very weak anomaly near $T_N \sim 15$ K is identifiable in the C_P/T^2 plot, as shown in the inset of Fig. 5(a). Peak temperatures identified by the broad maxima and the weak anomaly are consistent to those observed in $\chi(T)$ and $d\chi/dT(T)$ plots shown in Fig. 3.

Since the nonmagnetic Ba_2ZnTeO_6 compound has a different crystal structure [26], the absence of a nonmagnetic isomorphic compound for Ba_2CuTeO_6 does not allow a direct deduction of the lattice contribution (C_L) accurately. The magnetic contribution of specific heat (C_m) was roughly estimated using a Debye T^3 law approximation. The heat-capacity data above T_N are well fitted to $C_P/T = \gamma + \beta T^2$ with $\gamma = 24 \times 10^{-3}$ J/(mol K) and $\beta = 8.13 \times 10^{-4}$ J/(mol K^4). Since Ba_2CuTeO_6 is an insulator, it is reasonable to assign the linear term γT to the magnetic contribution (C_m), as expected for a homogeneous spin-$\frac{1}{2}$ chain system [43], and the βT^3 term to the lattice contribution (C_L). Therefore, the magnetic contribution was calculated as $C_m = C_P - C_L$. The Debye temperature of 288.6 K can be estimated with the formula $\beta = 12\pi^4 Rn/(5\Theta_D^3)$, where R, n, and Θ_D are the gas constant, the number of atoms per formula unit (in this case $n = 10$), and the Debye temperature, respectively. The Debye temperature is consistent with those reported for the similar Cu-based systems [44,45].
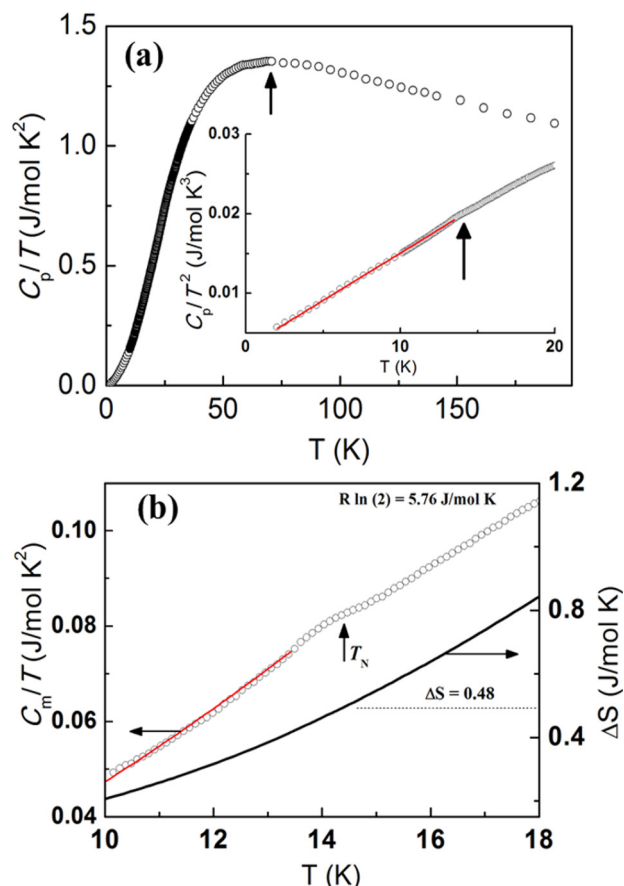
The magnitude of a small anomaly near $T_N \sim 15$ K is found to be more pronounced in the C_m/T vs T plot, as shown in Fig. 5(b). The entropy change (ΔS) was calculated by integrating the C_m/T as a function of temperature [$\Delta S = \int (C_m/T)dT$], as shown in Fig. 5(b). The entropy recovered at $T_N \sim 15$ K is about 0.48 J/(mol K), which is only about 8% of the total spin entropy of $R\ln 2 \sim 5.76$ J/(mol K) for the Cu $S = \frac{1}{2}$. From the estimation of ΔS, it is obvious that the amount of spin entropy change at T_N is too little to produce a sizable C_m feature like most quasi-2D systems [46], such as copper pyrazine (pz) perchlorate $Cu(pz)_2(ClO_4)_2$ [47].

According to the spin-wave (magnon) theory, the low temperatures C_m follow a $T^{d/n}$ behavior, where d is the dimensionality of the magnetic lattice and n is the exponent in the dispersion relation ($n = 1$ for antiferromagnets and $n = 2$ for ferromagnets) [48–50]. The spin-wave heat capacity of a 2D antiferromagnet is proportional to T^2 and a 3D antiferromagnet is proportional to T^3. The fittings of the C_P/T^2 and C_m/T data shown in Figs. 5(a) and 5(b) indicate that the C follows a $T^{d/n}$ dependence with fitted value of $d/n \sim 2.63$,
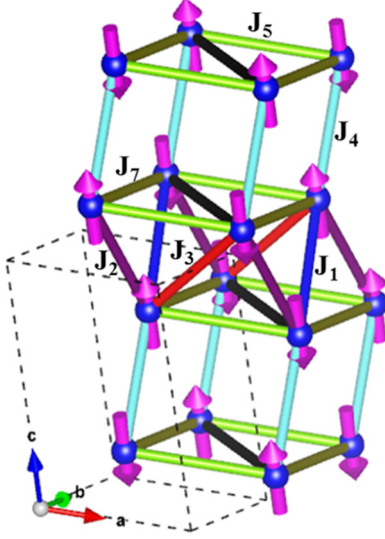
FIG. 6. Proposed spin arrangement for the configuration AF1 and exchange paths in Ba_2CuTeO_6, where different colors of cylinders represent different exchange parameters as tabulated in Table I, i.e., the major three nearest-neighbor exchange constants J_5, J_4, and J_1 are shown in colors of green, cyan, and blue, respectively.

which suggests the system could be viewed as a quasi-2D antiferromagnet with a relatively weak interplane coupling.

D. Theoretical calculations

Based on the geometric parameters associated with the paths for the Te-bridged SSE routes shown in Fig. 1(c), we considered seven exchange-coupling parameters $J_1 - J_7$ (see Fig. 6) as summarized in Table I. In order to find out the magnetic ground state of the system, we considered various magnetic configurations possible within the supercell. Of these, we selected eight spin configurations, i.e., seven AFM configurations AF1–AF7 including the AFM ground state and the ferromagnetic (FM) configuration for estimating the nearest-neighbor exchange-coupling parameters $J_1 - J_7$. The spin arrangements of these configurations can be decoded from Eqs. (3)–(10). Here, negative J implies parallel spin arrangement and positive J implies antiparallel spin arrangement. From the geometrical parameters, it seems that J_2 and J_3 are

TABLE I. Geometrical parameters of Ba_2CuTeO_6 associated with the Cu-O . . . O-Cu spin-exchange paths shown in Fig. 6.

J_{ij}	Cu-Cu (Å)	O...O (Å)	∠Cu-O...O (deg)	Bond color
J_1	5.2817	2.6049	133.207;129.423	Blue
J_2	5.3404	2.6225	137.021;126.321	Purple
J_3	5.3439	2.6049	133.880;127.653	Red
J_4	5.4616	2.7784	115.490;114.563	Cyan
		2.8146	118.073;118.316	Cyan
		2.8667	110.470;111.372	Cyan
J_5	5.7230	2.6905	139.141;137.807	Green
J_6	5.8553	2.8267	143.274;132.225	Black
J_7	5.8610	2.7236	144.879;132.555	Olive

TABLE II. Calculated total energy ΔE (relative to the total energy of FM state $E_{FM} = -56.4524$ eV/f.u.), total magnetic moment m_s^{tot}, atomic moment of Cu m_s^{Cu}. Note that one supercell contains 16 f.u.

Config.	ΔE (meV/f.u.)	m_s^{tot} (μ_B/f.u.)	m_s^{Cu} (μ_B/atom)
FM	0.0	1.0	0.70
AF1	−10.12	0.0	0.70
AF2	−9.40	0.0	0.70
AF3	−7.23	0.0	0.70
AF4	−7.04	0.0	0.70
AF5	−6.37	0.0	0.70
AF6	−6.10	0.0	0.70
AF7	−2.63	0.0	0.70

very similar and one may consider them to be same. The same is true for J_6 and J_7. But, from our calculations, we found that these two couplings are quite different. For example, spin configuration AF1 [Eq. (4)] and AF2 [Eq. (5)] have opposite orientations for the spins coupled via J_2, J_3, J_6, and J_7, while the rest spin orientations are the same. However, the total energy of AF1 is 0.72 meV/f.u. lower than that of AF2 state (Table II). Similarly, spin configurations AF3 [Eq. (6)] and AF4 [Eq. (7)] differ by the spin orientation of J_2, J_3, J_6, and J_7 (the rest of the spin orientations are same), have a total energy difference of 0.19 meV/f.u. (Table II). Thus, J_2, J_3, J_6, and J_7 must be distinguishable.

The relative energies of these eight spin configurations (seven AFM configurations AF1–AF7 and one FM configuration) calculated by DFT+U are summarized in Table II. We find that configuration AF1 has the lowest energy and thus we have the AF ground state consistent with the experimental finding. The magnetic moment of copper ion was found to be $0.7\mu_B$, slightly off to the $1\mu_B$ value as required by Cu^{2+} oxidation state, suggesting that some of the magnetic moments lie outside the copper atomic sphere used.

To extract the values of $J_1 - J_7$, we expressed the total spin exchange interaction energies of the Ba_2CuTeO_6 in terms of spin Heisenberg Hamiltonian $H = E_0 - \sum_{\langle ij \rangle} J_{ij}\sigma_i \cdot \sigma_j$. Here, J_{ij} is the exchange interaction parameter between the nearest-neighbor Cu site i and site j; and σ_i (σ_j) is the unit vector representing the direction of the local magnetic moment at site i (j). For AF interaction, $J < 0$ is assumed and for FM interaction, $J > 0$. The constant E_0 contains all spin-independent interactions.

The total energies of the supercell of all considered magnetic configurations are given by

$$E_{FM} = E_0 - 8(J_1 + J_2 + J_3 + J_4 + J_5 + J_6 + J_7), \quad (3)$$

$$E_{AF1} = E_0 + 8(J_1 - J_2 + J_3 + J_4 + J_5 - J_6 + J_7), \quad (4)$$

$$E_{AF2} = E_0 + 8(J_1 + J_2 - J_3 + J_4 + J_5 + J_6 - J_7), \quad (5)$$

$$E_{AF3} = E_0 - 8(J_1 - J_2 + J_3 - J_4 - J_5 + J_6 - J_7), \quad (6)$$

$$E_{AF4} = E_0 - 8(J_1 + J_2 - J_3 - J_4 - J_5 - J_6 + J_7), \quad (7)$$

$$E_{AF5} = E_0 + 8(J_1 + J_2 - J_3 - J_4 + J_5 + J_6 - J_7), \quad (8)$$

TABLE III. Calculated exchange interaction parameters (in K).

J_1/k_B	J_2/k_B	J_3/k_B	J_4/k_B	J_5/k_B	J_6/k_B	J_7/k_B
−30.46	−1.10	−4.17	−35.12	−45.01	2.63	−2.64

$$E_{AF6} = E_0 + 8(J_1 + J_2 + J_3 + J_4 - J_5 - J_6 - J_7), \quad (9)$$

$$E_{AF7} = E_0 + 8(J_1 - J_2 - J_3 - J_4 - J_5 + J_6 + J_7). \quad (10)$$

Solving the above-mentioned equations, we get the values of all exchange interactions listed in Table III. It is found that the face-shared Cu-Te2-Cu dimer (J_4) and the two corner-shared Cu-Te1-Cu dimer (J_1 and J_5) couplings are the strongest. These AF exchange couplings are found to be $J_5/k_B = -45.01$ K, $J_4/k_B = -35.12$ K, and $J_1/k_B = -30.46$ K [Figs. 6 and 1(c)]. J_2 is smallest among all the couplings and hence it is overruled by all other couplings in the ground state AF1.

We found that there is a large variation in the values of exchange parameters. For some set of the fitted coupling values, it varies by an order of magnitude, e.g., J_2, J_3, J_6, and J_7. At intermediate temperatures, it is expected that some of the weak couplings might be easily destroyed by the thermal fluctuations in the system. Hence, the resulting magnetic structure must be dominated by the three largest couplings of J_5, J_4, and J_1, which strongly suggests a spin system of a spin chain system with two nearly equal interchain couplings, as indicated by the T_{max} short-range spin-exchange correlation from $\chi(T)$ (see Fig. 3) and $C_P(T)$ (see Fig. 5) measurements.

In Fig. 7, we plotted the band structure (top panel) and density of states (bottom panel) of configuration AF1. The conduction band has very low dispersion as it has a dominant $3d$ character of copper atoms. From the atom-resolved density of states, it is quite clear that the valence band consists of hybridized oxygen $2p$ (p_z and p_y) and copper $3d_{yz}$ states. On the other hand, the conduction band has the dominant contribution from the very narrow copper d_{xz} band and a small contribution from oxygen p_z and p_x states. The Ba_2CuTeO_6 is an AF insulator with a band gap of 1.0 eV.

Based on the crystal structure which can be simplified as a Te-bridged CuO_6 octahedra, the magnetic structure is expected to be determined by the SSE coupling between the Cu spins via the Cu-O-Te1-O-Cu path for J_5 and J_1, and the Cu-O-Te2-O-Cu path for J_4 [Fig. 1(c)]. To justify the accuracy of the theoretical values of coupling constants, we can estimate the Curie-Weiss temperature Θ in terms of the fitted coupling parameters $J_1 - J_7$ [51]. In the mean-field approximation, which is valid only in the paramagnetic limit, Θ is related to the J_i as

$$\Theta = \frac{S(S+1)}{3k_B} \sum_i z_i J_i.$$

Where the summation runs over all the nearest neighbors of a given spin site, z_i is the number of nearest neighbors connected by the spin-exchange parameters J_i and S is the spin quantum number of each spin ($S = \frac{1}{2}$ for Cu atom). The calculated Θ value using the parameters obtained from
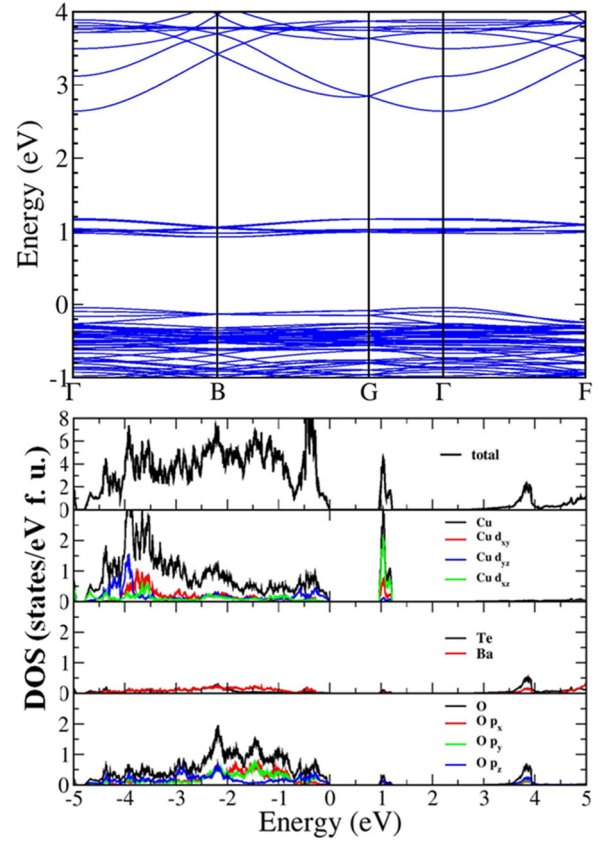

FIG. 7. Band structure (top panel) and density of states (bottom panel) of configuration AF1. Top of the valence band has been set to zero.

GGA+U calculations is -57.94 K, which agrees very well with the experimental value of -63 K from the Curie-Weiss law fitting discussed above.

E. Te-bridged spin chain and spin dimer

The spin-chain system having two different interchain couplings has been found in many cuprate compounds experimentally, and these compounds can be viewed as a two-leg spin ladder theoretically [52–55]. The spin-$\frac{1}{2}$ even-leg ladders are expected to have a spin-liquid ground state with short-range spin correlations [12,56,57]. On the other hand, when couplings between the ladders are not negligible, the system exhibits long-range ordering at finite temperature [58,59]. It is interesting to note that indeed the current system can also be described as a two-leg spin ladder system with intrachain coupling J_5 along the two legs of a spin ladder, interchain coupling J_4 as the rung of a two-leg ladder, and an interladder coupling J_1. The J_5 intrachain coupling has a SSE route through Te(1)-bridged CuO_6 octahedra via corner-sharing oxygens, J_4 is SSE route through Te(2)-bridged CuO_6 octahedra with face-shared oxygens, and J_1 is also a Te(1)-bridged SSE route via oxygen corner sharing as shown in Fig. 8(a). Once the 2D AF correlation is built up to certain correlation length, weak effective exchange interaction between the spin ladder planes will give rise to the AF long-range ordering of T_N at low temperature, which is
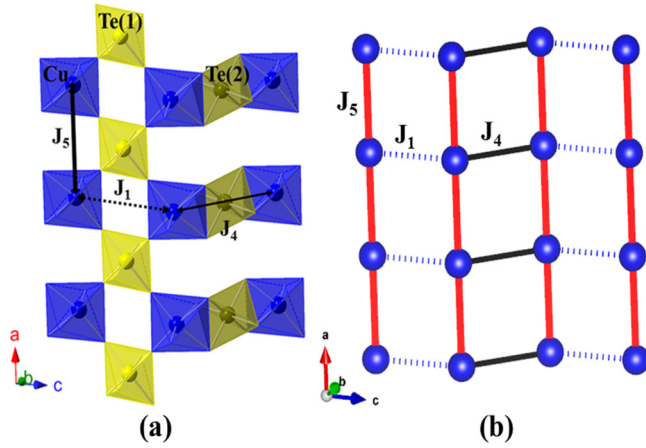
FIG. 8. (a) The layer of two-leg Cu spin ladder [see also Fig. 1(c)] formed via SSE mechanism, including the Te(1)-bridged spin chain as the leg of a ladder along J_5 (Cu-Te1-Cu), Te(2)-bridged spin dimer as the rung of a ladder along J_4 (Cu-Te2-Cu), and the Te(1)-bridged interladder coupling along J_1 (Cu-Te1-Cu). (b) The corresponding schematic illustration of the three parameters of a two-leg spin ladder.

supported from the weak "interplane" couplings of J_i ($i = 2$, 3, and 7) which are one order smaller than the couplings of J_i ($i = 5$, 4, and 1) responsible for the two-leg spin ladder plane, as shown in Table III and Fig. 8(b) [52,60].

The spin configuration of Ba_2CuTeO_6 has been implied to be a two-leg ladder based on both the structure aspect shown in Fig. 1(c) and the calculated magnetic coupling constants shown in Table III, as also compared in Fig. 8. Unlike the conventional Cu-O-Cu spin superexchange (SE) interaction discussed in the high-T_c cuprate systems, all Cu^{2+} spins are coupled via a super superexchange (SSE) route through either Cu-O-Te1-O-Cu or Cu-O-Te2-O-Cu paths [Fig. 1(b)]. It is also interesting to note that structurally the Cu-O-Te1-O-Cu path corresponds to the oxygen corner-sharing among CuO_6 and $Te(1)O_6$ octahedra, on the other hand, the Cu-O-Te2-O-Cu path corresponds to face-sharing octahedra between the two, as shown in Fig. 1(c). The strength of a spin-exchange interaction between two adjacent Cu^{2+} ions through SSE paths has been shown depending mostly on the orbital overlap of the two O-$2p$ orbitals and the two Cu-d orbitals [61,62]. These orbitals' overlap seems to increase with larger $\angle$Cu-O...O bond angles and shorter O...O distances, especially must be shorter than the van der Waals radii sum ~3.04 Å [63,64]. The reason that J_5 is the strongest (see Table III) can be understood from the fact that O_5...O_6 bond length of 2.6905 Å is significantly shorter than the van der Walls distance, and both $\angle$Cu-O...O bond angles of 137.807° and 139.141° are larger comparing to those of J_4 and J_1 with the SSE path. On the other hand, even J_1 has a shorter O...O distance and larger $\angle$Cu-O...O bond angles comparing with those of J_4, the SSE path of J_4 corresponds to the face-shared CuO_6-TeO_6 octahedra having three O...O routes of bond distances ~2.7785, 2.8146, and 2.8667 Å, the overlap integrals of J_4 are stronger than that

of the path J_1 [65]. While modified Kanamori-Goodenough rules for the SSE mechanism have been proposed by Whangbo *et al.* with some verified examples and supported partly by the current *ab initio* calculations [61,62], it is clear that the number of O...O paths, i.e., oxygen corner sharing or face sharing, must be taken into account in addition to the rules generated earlier, i.e., considering only on the O...O distance and $\angle$Cu-O...O bond angles for the spin SSE mechanism.

Based on the current calculations, the strongest spin-exchange interaction J_5 supports the spin-chain formation as the leg of a two-leg spin ladder, and the second strongest J_4 ($J_4/J_5 = 0.78$) could be viewed to support the rung of a two-leg spin ladder, and J_1 ($J_1/J_5 = 0.67$) introduces a frustrating interladder AF coupling which is slightly weaker than that of J_4, as shown in Fig. 8(b). This two-leg spin ladder with significant interladder couplings forms a plane and is responsible for the observed broad maximum near T_{max} due to the spin-exchange coupling in short range due to the low dimensionality. At temperatures below T_N of less thermal fluctuation, the much weaker AF interlayer couplings of J_i ($i = 7$, 3, and 2) could induce the observed AF long-range orderings, as observed in both $\chi(T)$ (see Fig. 3) and $C_P(T)$ (see Fig. 5).

IV. SUMMARY AND CONCLUSION

The crystal growth and magnetic and thermodynamic properties of Ba_2CuTeO_6 with triclinic symmetry are reported. The observed experimental and theoretical results provide the picture of a two-leg spin ladder system that evolves from a short-range intrachain spin interactions and to the long-range ordered 3D AF ordering in steps. In particular, the Cu spins are of SSE coupling mechanism via Cu-O-Te-O-Cu route. The magnetic susceptibility $\chi(T)$ data and its derivative $d\chi/dT$ show signature of spin-exchange coupling of short-range AF nature at $T_{max} \sim 75$ K in $\chi(T)$, before the system is ultimately driven into a 3D LRO below $T_N = 15$ K. The isothermal magnetization for $H \perp ab$ plane reveal a spin-flop transition with $H \sim 15$ kOe to confirm the existence of a 3D AF LRO below T_N with spin anisotropy along the c direction. The heat capacity C_P of the Ba_2CuTeO_6 single crystal is also found consistent to the proposed spin structure of a two-leg spin ladder with significant interladder coupling in 2D. A neutron diffraction study to the title compound is underway to solve the AF spin structure below T_N. This study is valuable to the understanding of both spin ladder and spin coupling in SSE route.

[1] J. M. Tranquada, B. J. Sternlieb, J. D. Axe, Y. Nakamura, and S. Uchida, Nature (London) **375**, 561 (1995).

[2] M. K. Wu, J. R. Ashburn, C. J. Torng, P. H. Hor, R. L. Meng, L. Gao, Z. J. Huang, Y. Q. Wang, and C. W. Chu, Phys. Rev. Lett. **58**, 908 (1987).

[3] P. W. Anderson, Science **235**, 1196 (1987).

[4] N. Read and S. Sachdev, Phys. Rev. Lett. **62**, 1694 (1989).

[5] F. Becca and F. Mila, Phys. Rev. Lett. **89**, 037204 (2002).

[6] Z. Y. Weng, D. N. Sheng, C. S. Ting, and Z. B. Su, Phys. Rev. Lett. **67**, 3318 (1991).

[7] E. H. Lieb and F. Y. Wu, Phys. Rev. Lett. **20**, 1445 (1968).

[8] H. Fujisawa, T. Yokoya, T. Takahashi, S. Miyasaka, M. Kibune, and H. Takagi, Phys. Rev. B **59**, 7358 (1999).

[9] R. Neudert, M. Knupfer, M. S. Golden, J. Fink, W. Stephan, K. Penc, N. Motoyama, H. Eisaki, and S. Uchida, Phys. Rev. Lett. **81**, 657 (1998).

[10] M. Hase, I. Terasaki, and K. Uchinokura, Phys. Rev. Lett. **70**, 3651 (1993).

[11] M. Uehara, T. Nagata, J. Akimitsu, H. Takahashi, N. Mori, and K. Kinoshita, J. Phys. Soc. Jpn. **65**, 2764 (1996).

[12] M. Azuma, Z. Hiroi, M. Takano, K. Ishida, and Y. Kitaoka, Phys. Rev. Lett. **73**, 3463 (1994).

[13] K. R. Thurber, T. Imai, T. Saitoh, M. Azuma, M. Takano, and F. C. Chou, Phys. Rev. Lett. **84**, 558 (2000).

[14] H. Kotegawa, Y. Tokunaga, Y. Araki, G.-q. Zheng, Y. Kitaoka, K. Tokiwa, K. Ito, T. Watanabe, A. Iyo, Y. Tanaka, and H. Ihara, Phys. Rev. B **69**, 014501 (2004).

[15] I. P. Muthuselvam, R. Sankar, V. Nand Singh, G. Narsinga Rao, W. L. Lee, G. Y. Guo, and F. C. Chou, Inorg. Chem. **54**, 4303 (2015).

[16] G. Blasse, Philips Res. Rep. **20**, 327 (1965).

[17] D. Iwanaga, Y. Inaguma, and M. Itoh, J. Solid State Chem. **147**, 291 (1999)

[18] S. Vasala and M. Karppinen, Prog. Solid State Chem. **43**, 1 (2015).

[19] W. Levason, M. D. Spicer, and M. Webster, J. Chem. Soc., Dalton Trans. **5**, 1377 (1988).

[20] W. Levason, Coord. Chem. Rev. **161**, 33 (1997).

[21] R. Yu, K. M. Ok, and P. S. Halasyamani, Dalton Trans. **3**, 392 (2004).

[22] T. Koga, N. Kurita, and H. Tanak, J. Phys. Soc. Jpn. **83**, 115001 (2014).

[23] J. Xu, A. Assoud, N. Soheilnia, S. Derakhshan, H. L. Cuthbert, J. E. Greedan, M. H. Whangbo, and H. Kleinke, Inorg. Chem. **44**, 5042 (2005).

[24] R. Sankar, I. P. Muthuselvam, G. J. Shu, W. T. Chen, S. K. Karna, R. Jayavel, and F. C. Chou, CrystEngComm **16**, 10791 (2014).

[25] J. Yeon, S.-H. Kim, M. A. Green, K. P. Bhatti, C. Leighton, and P. S. Halasyamani, J. Solid State Chem. **196**, 607 (2012).

[26] Von P. Kohl and D. Reinen, Z. Anorg. Allg. Chem. **409**, 257 (1974).

[27] P. E. Blöchl, Phys. Rev. B **50**, 17953 (1994).

[28] G. Kresse and J. Hafner, Phys. Rev. B **47**, 558 (1993).

[29] G. Kresse and J. Furthmüller, Comput. Mater. Sci. **6**, 15 (1996).

[30] J. P. Perdew, K. Burke, and M. Ernzerhof, Phys. Rev. Lett. **77**, 3865 (1996).

[31] S. L. Dudarev, G. A. Botton, S. Y. Savrasov, C. J. Humphreys, and A. P. Sutton, Phys. Rev. B **57**, 1505 (1998).

[32] C. L. Chen, K. W. Yeh, D. J. Huang, F. C. Hsu, Y. C. Lee, S. W. Huang, G. Y. Guo, H.-J. Lin, S. M. Rao, and M. K. Wu, Phys. Rev. B **78**, 214105 (2008).

[33] A. C. Larson and R. B. Von Dreele, General Structure Analysis System (GSAS), Los Alamos National Laboratory Report No. LAUR 86-748, 2004 (unpublished).

[34] J. Rossat-Mignot, L. P. Regnault, P. Bourges, P. Burlet, C. Vettier, and J. Y. Henry, *Selected Topics in Superconductivity*, Frontiers in Solid State Sciences, edited by L. C. Gupta and M. S. Multani, Vol. 1 (World Scientific, Singapore, 1993), p. 265.

[35] H. D. Zhou, E. S. Choi, G. Li, L. Balicas, C. R. Wiebe, Y. Qiu, J. R. D. Copley, and J. S. Gardner, Phys. Rev. Lett. **106**, 147204 (2011).

[36] P. W. Selwood, *Magnetochemistry*, 2nd ed. (Wiley-Interscience, New York, 1956), Chap. 2, p. 78.

[37] R. Nath, A. V. Mahajan, N. Büttgen, C. Kegler, A. Loidl, and J. Bobroff, Phys. Rev. B **71**, 174436 (2005).

[38] N. Motoyama, H. Eisaki, and S. Uchida, Phys. Rev. Lett. **76**, 3212 (1996).

[39] S. Lebernegg, A. A. Tsirlin, O. Janson, R. Nath, J. Sichelschmidt, Yu. Skourski, G. Amthauer, and H. Rosner, Phys. Rev. B **84**, 174436 (2011).

[40] J. C. Bonner and M. E. Fisher, Phys. Rev. **135**, A640 (1964).

[41] W. E. Estes, D. P. Gavel, W. E. Hatfield, and D. J. Hodgson, Inorg. Chem. **17**, 1415 (1978).

[42] L. Néel, Ann. Phys. (Paris) **5**, 232 (1936).

[43] T. Wei, A. J. Heeger, M. B. Salamon, and G. E. Delker, Solid State Commun. **21**, 595 (1977).

[44] Y. P. Feng, A. Jin, D. Finotello, K. A. Gillis, M. H. W. Chan, and J. E. Greedan, Phys. Rev. B **38**, 7041 (1988).

[45] K. Fabricius, A. Klümper, U. Löw, B. Büchner, T. Lorenz, G. Dhaleene, and A. Revcolevschi, Phys. Rev. B **57**, 1102 (1998).

[46] P. Sengupta, A. W. Sandvik, and R. R. P. Singh, Phys. Rev. B **68**, 094423 (2003).

[47] T. Lancaster, S. J. Blundell, M. L. Brooks, P. J. Baker, F. L. Pratt, J. L. Manson, M. M. Conner, F. Xiao, C. P. Landee, F. A. Chaves, S. Soriano, M. A. Novak, T. P. Papageorgiou, A. D. Bianchi, T. Herrmannsdörfer, J. Wosnitza, and J. A. Schlueter, Phys. Rev. B **75**, 094421 (2007).

[48] L. J. de Jongh and A. R. Miedema, *Experiments on Simple Magnetic Model Systems* (Taylor and Francis, London, 1974).

[49] L. J. de Jongh and A. R. Miedema, Adv. Phys. **23**, 1 (1974).

[50] M. Sorai, Y. Nakazawa, M. Nakano, and Y. Miyazaki, Chem. Rev. **113**, PR41 (2013).

[51] J. S. Smart, *Effective Field Theory of Magnetism* (Saunders, Philadelphia, 1996).

[52] M. Azuma, Y. Fujishiro, M. Takano, M. Nohara, and H. Takagi, Phys. Rev. B **55**, R8658 (1997).

[53] E. Dagotto, Rep. Prog. Phys. **62**, 1525 (1999).

[54] E. Dagotto and T. M. Rice, Science **271**, 618 (1996).

[55] S. Sachdev, Nat. Phys. **4**, 173 (2008).

[56] Z. Hiroi, M. Azuma, M. Takano, and Y. Bando, J. Solid State. Chem. **95**, 230 (1991).

[57] Y. Kohama, S. Wang, A. Uchida, K. Prsa, S. Zvyagin, Yu. Skourski, R. D. McDonald, L. Balicas, H. M. Ronnow, C. Ruegg, and M. Jaime, Phys. Rev. Lett. **109**, 167204 (2012).

[58] B. Normand and T. M. Rice, Phys. Rev. B **54**, 7180 (1996).

[59] K.-Y. Choi, J. W. Hwang, P. Lemmens, D. Wulferding, G. J. Shu, and F. C. Chou, Phys. Rev. Lett. **110**, 117204 (2013).

[60] S. Wessel and S. Haas, Phys. Rev. B **62**, 316 (2000).

[61] M.-H. Whangbo, H.-J. Koo, and D. Dai, J. Solid State Chem. **176**, 417 (2003).

[62] M.-H. Whangbo, D. Dai, and H.-J. Koo, Solid State Sci. **7**, 827 (2005).

[63] R. Bertani, P. Sgarbossa, A. Venzo, F. Lelj, M. Amati, G. Resnati, T. Pilati, P. Metrangolo, and G. Terraneo, Coord. Chem. Rev. **254**, 677 (2010).

[64] H.-J. Koo and M.-H. Whangbo, Inorg. Chem. **47**, 128 (2008).

[65] H. W. Bae and H.-J. Koo, Bull. Korean Chem. Soc. **29**, 122 (2008).